Unexpected product fine-structure distributions in (3+1)-photon ionization of xenon

C. Bordas,* M. J. Dyer, T. Fairfield, and H. Helm
Molecular Physics Laboratory, SRI International, Menlo Park, California 94025

K. C. Kulander
Joint Institute for Laboratory Astrophysics, University of Colorado at Boulder, Boulder, Colorado 80309
and Lawrence Livermore National Laboratory, Livermore, California 94551

(Received 25 April 1994)

Three-photon resonance enhanced four-photon ionization of xenon shows preferential formation of $Xe^+(^2P_{1/2})$ when intermediate $ns[3/2]_1$ Rydberg states are excited in the three-photon step. Here, the $nl[K]_J$ notation refers to $j_c l$ coupling, in which the angular momentum of the ion core, j_c, is coupled to the orbital angular momentum of the Rydberg electron l to give K, which is then coupled to the Rydberg electron's spin to give J. The primes following l denote states belonging to the $^2P_{1/2}$ core. Multichannel-quantum-defect theory identifies these intermediates as nearly pure Rydberg states belonging to the $Xe^+(^2P_{3/2})$ core. An equivalent behavior is found for the $7s'[1/2]_1$ intermediate state which preferentially produces $Xe^+(^2P_{3/2})$. On the other hand, for nd and nd' resonances we observe final-state distributions which closely mirror the core character of the intermediate state. The suppression of the parent core channel for s-type Rydberg states is shown to be due to a Cooper minimum in the $ns \rightarrow \varepsilon p$ transition amplitudes. As a consequence, minor components of the resonance state wave functions play a major role in the selection of the final ionization channel, in particular via the much larger amplitudes of $nd' \rightarrow \varepsilon f'$ transitions.

PACS number(s): 33.80.−b

INTRODUCTION

Several recent studies of the heavier rare gases have examined the role that intermediates play in resonant enhancement of the photoionization rate [1-4]. If the resonantly enhanced N-photon ionization process is formally separated into an $(N-1)$-photon excitation step to the resonant state, followed by one-photon ionization, one may expect that the formation of ionic states should largely depend on the electronic structure of the resonant state. Indeed Sato, Achiba, and Kimura [2] observed the formation of only ground-state ions for ionization via the Xe $5d[5/2]_3$ state, which is nearly a pure Rydberg state on the $Xe^+(^2P_{3/2})$ core. In a similar case, Matthias *et al.* found that the branching ratios into the $6s$ and $5d$ continua of Ba^+ are correlated with the configuration mixing in the Rydberg states from which ionization takes place [5].

We have investigated the effects of intermediate resonances on multiphoton ionization of xenon by examining the final-state distribution and the respective angular distributions of photoelectrons for 25 three-photon intermediates that participate in four-photon ionization in xenon. For the nd and nd' intermediate states we find that the observed branching between the two final ion channels correlates with the configuration mixing in the excited states predicted by multichannel-quantum-defect theory (MQDT). A major deviation from this rule appears for the $ns[3/2]_1$ states. These states are predicted to be nearly pure $Xe^+(^2P_{3/2})$ Rydberg states, yet (3+1)-photon ionization via these states leads preferentially to the formation of the $Xe^+(^2P_{1/2})$ ion. A similar preference for the opposite core channel is observed for the $7s'[1/2]_1$ state which preferentially produces $Xe^+(^2P_{3/2})$.

An explanation for the preference of the $Xe^+(^2P_{1/2})$ channel in resonance-enhanced multiphoton ionization (REMPI) via the ns-Rydberg members is found in numerical calculations of the one-photon transition amplitudes which predict the appearance of a Cooper minimum for $ns \rightarrow kp$ transitions. This allows minor components of the $ns[3/2]_1$ state wave functions to play a major role in the selection of the ionization channel.

EXPERIMENT AND RESULTS

The experiments are carried out at near-threshold intensities (1–5 GW/cm^2) using a nanosecond dye laser (bandwidth 0.5 cm^{-1}) tuned to selectively excite the $J=1$ and $J=3$ resonances of xenon that lie between the $5d[7/2]_3$ and $7s'[1/2]_1$ states. A photoelectron imaging spectrometer [6] was used to measure the relative ionization yield in the final-state channels, $Xe^+(^2P_{1/2})$ and $Xe^2(^2P_{3/2})$, as well as the angular distribution of photoelectrons in either channel.

The operation of the imaging spectrometer is as follows: When photoelectrons are formed with a constant energy, in the focal region of the laser at time $t=0$, they are later found on the surface of an expanding sphere around the focal position. An external electric field can be applied to project this sphere onto a screen. This results in a circular image of electron impacts with a diameter that is related to the electron energy and a filling pattern that reveals the spatial distribution of the electrons on the surface of the sphere. Many electrons have to be

*Permanent address: Laboratoire de Spectrométrie Ionique et Moléculaire, Université Lyon I, France.

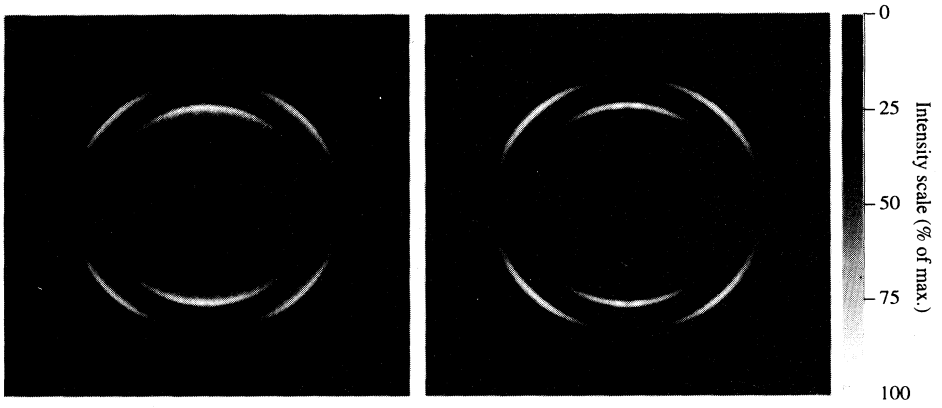

FIG. 1. Typical photoelectron image from four-photon ionization of xenon. The resonant intermediate in this case is $8d[1/2]_1$. The raw photoelectron image is shown on the left. The image on the right is the Abel-inverted image which shows the angular distribution of electrons. The radial coordinate is a measure of the electron velocity. The laser polarization is vertical, parallel to the screen.

projected in order to represent a statistically meaningful image. This is accomplished by digital summing of electron impact positions from several thousand laser shots, each shot capturing typically 10–100 electrons. The screen image is monitored with a charge coupled device (CCD) camera, digitized after each laser shot with 8-bit intensity resolution and transferred to computer memory where the summed image is accumulated.

In the current experiments a dc electric field of typically 50 V/cm was applied for projection of the electrons. We examined the dependence of the electron images on the magnitude of the applied field. No systematic changes were noted in the range from 30 to 150 V/cm, suggesting that our data are not influenced by dc Stark effects.

A primary interest in the current study is the branching between the two final ion channels $Xe^+(^2P_{1/2})$ and $Xe^+(^2P_{3/2})$. The difference in ionization potential between the two states amounts to 1.31 eV. Hence, electrons formed in the ground-state ion channel are created with a kinetic energy which is 1.31 eV higher than electrons formed in the excited ion channel. The electrons thus arrange on two concentric spheres, resulting in concentric circular images on the screen. An example of a raw experimental image is shown on the left-hand side of Fig. 1. The three-photon intermediate state accessed in this experiment is the $8d[1/2]_1$ level which is reached by three photons at a wavelength of 3168 Å. This image is recorded with the laser polarization parallel to the screen along the vertical direction. In the framework of electric dipole radiation, the electron emission pattern should be rotationally symmetric around the laser polarization [7]. This we have verified by recording images with the laser polarization pointing towards the screen. As a consequence of this symmetry, the images can be deconvoluted by an Abel inversion [8] giving directly the velocity and angular distribution of photoelectrons.

Before carrying out the Abel inversion the center of the screen image has to be determined. Generally we use a numerical routine which finds the maximum of the function

$$S=\sum_p T(x_p,y_p)T^*(x_p,y_p)$$
$$=\sum_p T(x_p,y_p)T(2x_0-x_p,2y_0-y_p)\ , \qquad (1)$$

where T refers to the intensity of the original image at the pixel position specified by p, and T^* refers to that of an image obtained by mirroring the original at the trial center position (x_0,y_0). Upon finding the center, the four quadrants of the image are added for better statistical representation and are subjected to the Abel procedure. As a consequence, the inverted images are symmetric about the vertical and horizontal axes.

On the right-hand side in Fig. 1 we give the Abel inverted image for the $8d[1/2]_1$ transition. The radial coordinate represents the electron velocity and the intensity variation along a circular path shows the angular dis-

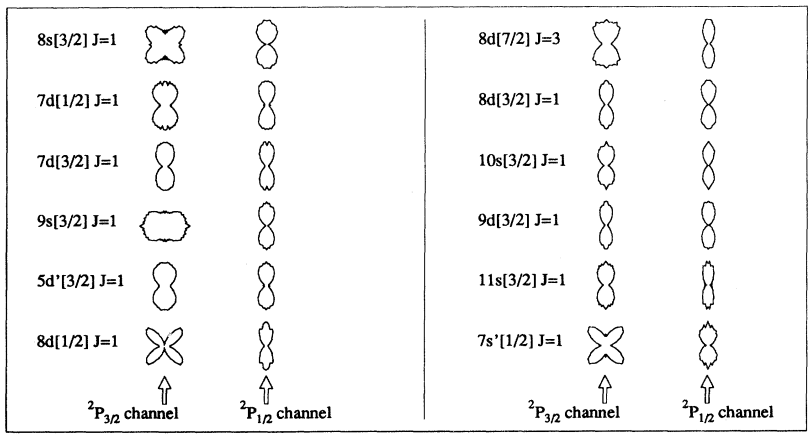

FIG. 2. Typical angular distributions and branching ratios for selected intermediate states. The laser polarization is along the vertical axis.

tribution. The outer ring structure refers to electrons formed in the $Xe^+(^2P_{3/2})$ channel, the inner to electrons formed in the $Xe^+(^2P_{1/2})$ channel.

We note substantially different angular emission patterns in the two final-state channels. Electrons populating the $Xe^+(^2P_{1/2})$ channel appear preferentially along the polarization axis while those in the $Xe^+(^2P_{3/2})$ channel show electrons being emitted preferentially at an angle of 45° with respect to the polarization axis. This drastic difference in angular distributions in the two ion channels is observed for the $7s'$, $8s$, $9s$, and $8d$ states, the remaining states showing less dramatic differences in the angular distributions. In Fig. 2 representative angular distributions are collected.

The detection efficiency of the imaging spectrometer is independent of electron energy, hence the branching among the two fine-structure channels can be determined with good precision by integrating over the respective electron signal. In Fig. 1, 39% of the total electron signal appears in the $Xe^+(^2P_{1/2})$ channel while 61% appear in the $Xe^+(^2P_{3/2})$ channel. Equivalent measurements were carried out for the ns states with $n=7$ to 11 and the nd states with $n=5$ to 9, as well as the $7s'$ and $5d'$ resonances. In Table I we compile the branching values measured in this experiment.

TABLE I. Branching ln(3+1)-photon REMPI of xenon. The observed fraction of ions in the $^2P_{1/2}$ channel is compared with the MQDT predicted core character M from Eq. (2). (nm = not measured.)

No.	Label	Energy (cm^{-1})	Obs.	M
1	$5d[7/2]_3$	80 970	0	0.038
2	$5d[5/2]_3$	82 430	0.005	0.002
3	$5d[3/2]_1$	83 890	0.093	0.151
4	$7s[3/2]_1$	85 440	0.57	0.007
5	$6d[1/2]_1$	88 550	0.38	0.101
6	$6d[7/2]_3$	89 025	0.23	0.099
7	$6d[5/2]_3$	89 535	0.064	0.005
8	$6d[3/2]_1$	90 032	0.55	0.213
9	$8s[3/2]_1$	90 932	0.62	0.006
10	$5d'[5/2]_3$	91 747	0.99	0.943
11	$7d[1/2]_1$	92 128	0.71	0.451
12	$7d[7/2]_3$	92 646	nm	0.413
13	$7d[3/2]_1$	92 714	0.70	0.511
14	$7d[5/2]_3$	92 734	nm	0.158
15	$9s[3/2]_1$	93 422	0.91	0.084
15a	$5g[7/2]_3, 5g[5/2]_3$		nm	
16	$5d'[3/2]_1$	93 619	0.91	0.741
17	$8d[1/2]_1$	94 228	0.39	0.292
18	$8d[7/2]_3$	94 291	0.27	0.087
19	$8d[5/2]_3$	94 371	0.15	0.006
20	$8d[3/2]_1$	94 686	0.69	0.452
21	$10s[3/2]_1$	94 787	0.63	0.063
21a	$6g[7/2]_3, 6g[5/2]_3$		nm	
22	$9d[1/2]_1$	95 228	nm	0.230
23	$9d[7/2]_3$	95 284	0.15	0.050
24	$9d[5/2]_3$	95 335	0.05	0.003
25	$9d[3/2]_1$	95 499	0.27	0.287
26	$11s[3/2]_1$	95 591	0.17	0.163
26a	$7g[7/2]_3, 7g[5/2]_3$		nm	
27	$7s'[1/2]_1$	95 801	0.25	0.966

DISCUSSION

The explicit form of the multiphoton ionization probability involves summation over an infinite number of virtual states, but is dominated by the resonant term [7]. The resonant term alone includes the summation over the angular terms and matrix elements of the dipole operator between all channels that contribute to the intermediate state configuration and all continuum channels ($J=0$ and $J=2$ for $J'=1$ intermediates and $J=2$ and $J=4$ for $J'=3$ intermediates). As a consequence, the configuration mixing in the three-photon excited intermediate from which ionization occurs should only in a first approximation be proportional to the branching in the respective $^2P_{3/2}$ and $^2P_{1/2}$ continua. Nevertheless, in cases where the intermediate state is characterized by a single, very dominant configuration, one would expect that this configuration plays a dominant role.

The configuration mixing can be evaluated in the framework of MQDT [9] using the semiempirical parameters derived previously [10,11]. For example, the $J=1$ Rydberg states include components corresponding to the following configurations $(^2P_{3/2}ns_{1/2})$, $(^2P_{3/2}nd_{3/2})$, $(^2P_{3/2}nd_{5/2})$, $(^2P_{1/2}ns'_{1/2})$, and $(^2P_{1/2}nd'_{3/2})$. The first three configurations lead to ionization into the lower continuum $^2P_{3/2}$ and the last two into the higher ion core $^2P_{1/2}$. Likewise, the $J=3$ Rydberg states include the configurations $(^2P_{3/2}nd_{5/2})$, $(^2P_{3/2}nd_{7/2})$, and $(^2P_{1/2}nd'_{5/2})$. The core character of the Rydberg state can be identified in terms of the sum of the squares of the respective amplitudes a_{nl_j} of the various nl_j-component wave functions. The MQDT calculated $^2P_{1/2}$ core character is defined as

$$M_1 = a^2_{ns'_{1/2}} + a^2_{nd'_{3/2}} \tag{2a}$$

for $J=1$ states and

$$M_3 = a^2_{nd'_{5/2}} \tag{2b}$$

for $J=3$ states.

In the last column in Table I we compare the $^2P_{1/2}$ core character with the observed fraction of ions appearing in the excited ion channel. The graphic comparison of the observed fraction of the ions in the $^2P_{1/2}$ state with the MQDT predicted $^2P_{1/2}$ core character in Fig. 3 shows that the final channel population mirrors closely the intermediate-state core character in the case of nd and nd' intermediates. The surprising observation is the branching among the final states when excitation occurs via the s-type Rydberg states. The MQDT analysis predicts that these states are nearly pure Rydberg states belonging to the $^2P_{3/2}$ core, yet ionization favors the $^2P_{1/2}$ final channel. For example, the $7s$ and $8s$ states are predicted to have an admixture of $^2P_{1/2}$ core of less than 1%, yet this core channel dominates the final products.

The apparent regularity with which the branching follows the core character for the d states but does not for the s states is not reflected in equivalent regularities of the angular distributions patterns. It is evident from the distributions in the $^2P_{3/2}$ continuum that in many in-

stances the angular part of the magnetic quantum number of the photoelectron shows substantial contributions from m values not equal to zero. This is not surprising. While we use linearly polarized light and start from a $J=0$ state, the requirement that the total M-quantum number of products to be zero can be met in a variety of m distributions of the core and electron momenta.

In searching for an explanation for the suppression of the parent core channel for the s states it appears natural to suspect a Cooper type minimum [12] in the cross section for the s component. Such minima are well documented for alkalis-metal atoms [13]. Theoretical predictions also exist for a Cooper minimum in the photoionization cross section of the metastable s states of the rare gases [14,15]. These calculations ignore spin-orbit mixing of the two cores and they predict an absolute zero in the cross section for Xe($6s$) and Xe($6s'$) at a photoelectron energy ε of ~ 1 eV.

A second observation, the ionization efficiency, suggests that a Cooper minimum need not be the sole explanation for the anomalous branching. The experimental ionization efficiency via the ns states is not particularly low, but rather most ns states stand out prominently in the photoionization spectrum. Figure 4 gives the wavelength dependence of a portion of our (3+1)-REMPI spectrum. The measured signal is not corrected for the wavelength dependence of the dye-laser output, but the actual laser energy is indicated in the figure as well.

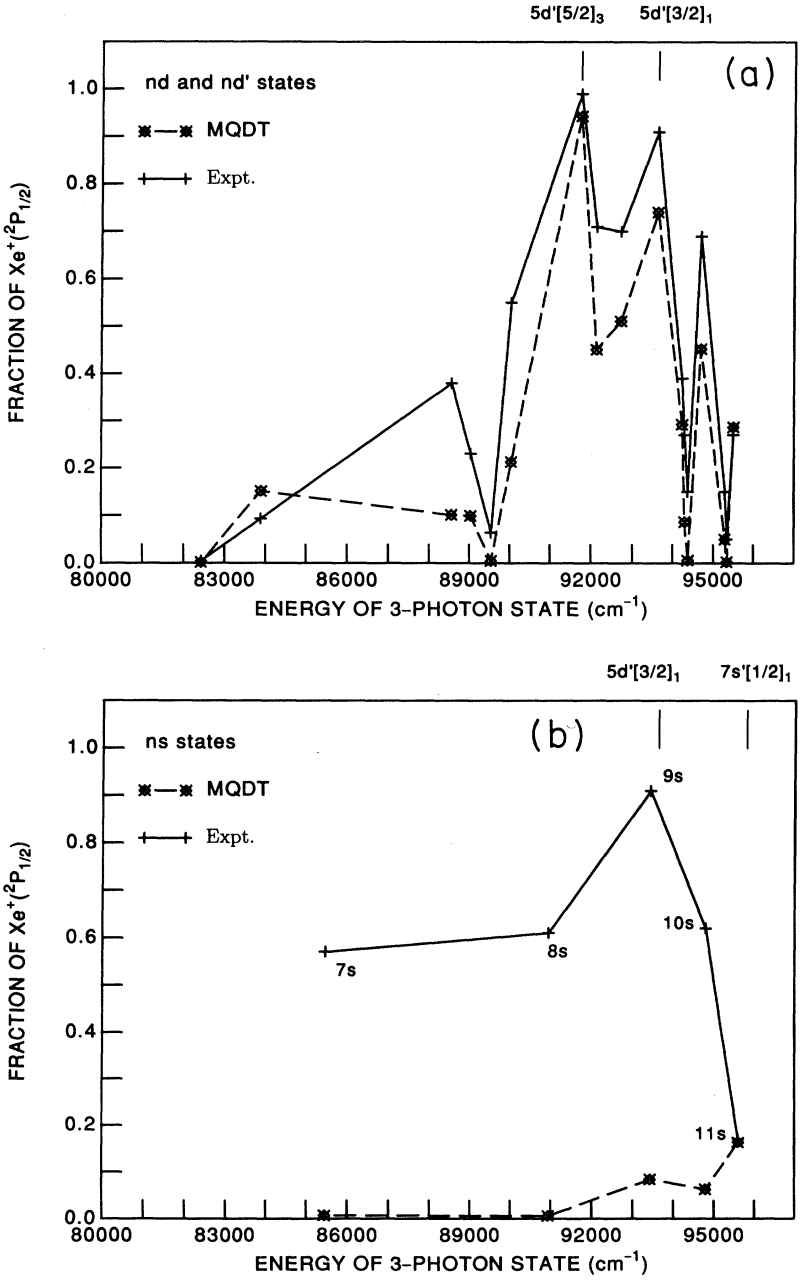

FIG. 3. Fraction of ions reaching $Xe^+(^2P_{1/2})$ following one-photon ionization of the three-photon excited ns, nd, and nd' states is shown by the open circles. The fractional $Xe^+(^2P_{1/2})$ core character predicted for these states by MQDT is shown by the full circles.

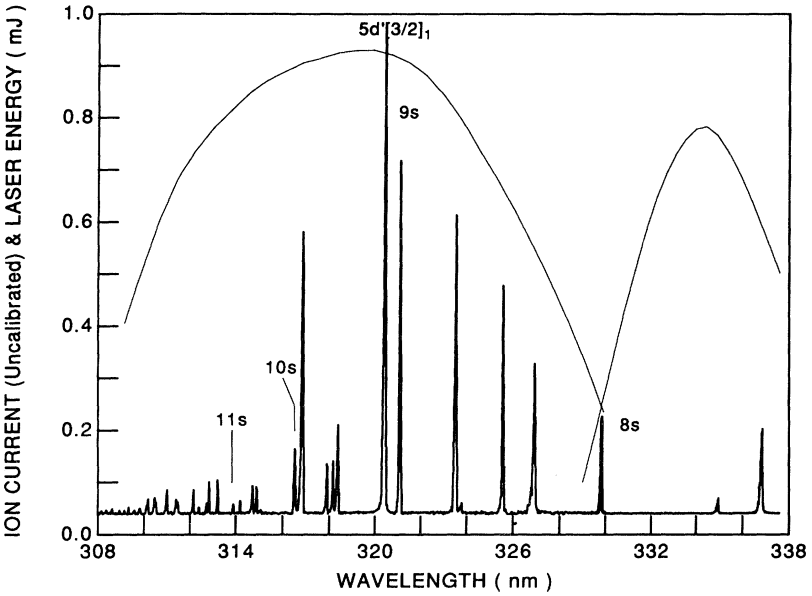

FIG. 4. Wavelength dependence of the uncorrected (3+1)-photon ionization signal in xenon. The laser intensity is displayed as well.

What is evident from this wavelength scan is that all transitions to s levels in the vicinity of the $5d'[3/2]_1$ resonance appear with enhanced intensity, anomalously strong in comparison with excitation via $11s$, the only s state which shows a branching commensurate with the MQDT core character. It appears as if the ns states borrow (3+1)-photon ionization intensity from the $5d'[3/2]_1$ state, indicative of giant resonance enhancement. To investigate such an explanation we have combined the MQDT predictions with calculations of the bound-free transition amplitudes from dominant components of the MQDT wave functions to assess the branching in the final-state ion channels.

In a search for an explanation of the anomalous branching one might also suspect that some of our measurements on the s states could be falsified due to unresolved contributions from the g states, which lie close in energy to the s states (see resonances labeled 15a, 21a, 26a in Table I). Pratt, Dehmer, and Dehmer [4] have resolved the autoionizing $13s'$ and $9g'$ states following three-photon excitation and they observed intensity of the g' transitions are much smaller than those to the s' state. Pertinent for our work is that the lowest possible g states $5g[7/2]_3$ and $5g[5/2]_3$ lie at the energy of the $9s[3/2]_1$ state. Hence the ionization signal via the $7s$ and $8s$ states cannot be contaminated by contributions from g states. Since the anomalous branching is also observed for $7s$ and $8s$, we consider the observed effect to be unrelated to g-state contamination of the experimental intensity.

THEORY OF PHOTOIONIZATION FROM ns-RYDBERG SERIES

In order to explain the anomalous behavior of the ns states we have carried out numerical calculations of the transition amplitudes to the ionization continuum. We are interested in the branching in photoionization of the $ns[3/2]_1$ levels with $n=7-11$ and the $7s'[3/2]_1$ state. Energy considerations then indicate the most likely interacting states are the nd states, with $n=6-9$ and $5d'$. The oscillator strength per unit atomic energy for ionization of these states is given by [16]

$$df^{ns}_{3/2}/d\varepsilon=(2/3)\hbar\omega_{ns}\{a^2_{ns_{1/2}}\langle ns|r|\varepsilon p\rangle^2+(2/5)[a^2_{nd_{3/2}}+a^2_{nd_{5/2}}]\langle nd|r|\varepsilon p\rangle^2+(3/5)[a^2_{nd_{3/2}}+a^2_{nd_{5/2}}]\langle nd|r|\varepsilon f\rangle^2\} \quad (3a)$$

and

$$df^{ns}_{1/2}/d\varepsilon'=(2/3)\hbar\omega_{ns}\{a^2_{7s'_{1/2}}\langle 7s'|r|\varepsilon p'\rangle^2+(2/5)a^2_{5d'_{3/2}}\langle 5d'|r|\varepsilon p'\rangle^2+(3/5)a^2_{5d'_{3/2}}\langle 5d'|r|\varepsilon f\rangle^2\}\ , \quad (3b)$$

where $\hbar\omega_{ns}=E_{ns}/3$, $\varepsilon=k^2/2m$ is the energy of the emitted electron, leaving the $^2P_{3/2}$-ion core and $\varepsilon'=\varepsilon-1.31$ eV, the continuum energy for the $^2P_{1/2}$ core.

In order to estimate the branching ratios between the two ionic continua we carried out numerical calculations of the dipole transition matrix elements,

$$\langle nl|r|\varepsilon l\pm1\rangle=\int_0^\infty P_{nl}(r)rF_{kl\pm1}(r)dr\ . \quad (4)$$

In our calculations we have included the $8d$ state and the $7s'$ for the ns series and the $11s$ and $8d$ states in calculation of the $7s'$ branching ratio.

The bound orbitals, P_{nl} are generated using a standard Hartree-Slater code which included the modification that the long-range tail of the effective potential becomes Coulombic outside the ion core [17]. The orbitals were obtained by adjusting slightly the strength, the $X\alpha$

coefficient of the (short-range) exchange-correlation term so that the binding energy of the lowest excited state for each orbital angular momentum l agrees with the observed value. This gives more accurate excitation energies and therefore presumably more accurate wave functions outside the range of the core. The continuum orbitals were obtained by numerical integration of the single-particle Schrödinger equation with the effective radial potential from the calculation for the lowest excited np state. We employed a fifth-order predictor-corrector algorithm for the integration. As the scattering orbitals were generated, the relevant dipole matrix elements were accumulated, then normalized when the asymptotic region was reached where the scattering states could be scaled to go asymptotically to

$$F_{kl} \sim (2/\pi k)^{1/2} \sin[kr - l\pi/2 + \delta_l + (1/k)\ln(2kr) + \arg\Gamma(l+1-i/k)] \, . \quad (5)$$

Here δ_l is the phase shift which is given in terms of the quantum defect $\pi\mu_l$.

The branching ratios into the different continua of the ion would follow those predicted by the MQDT amplitudes if the transition strengths for the different components were the same. This will not in general be the case, but here we find very surprising differences considering the ns components in each Rydberg state are so dominant. By calculating the one-photon ionization amplitudes for the component states of interest, we find that the reason the branching ratios are so severely altered is that the $ns \rightarrow \varepsilon p$ amplitudes are all approaching an almost common Cooper minimum for photon energies not too much larger than those used in the (3+1)-photon ionization process. Therefore these transition strengths are unusually small and the minor components of the resonance states then play a much larger role in defining the final-state branching ratios. We also find the interesting

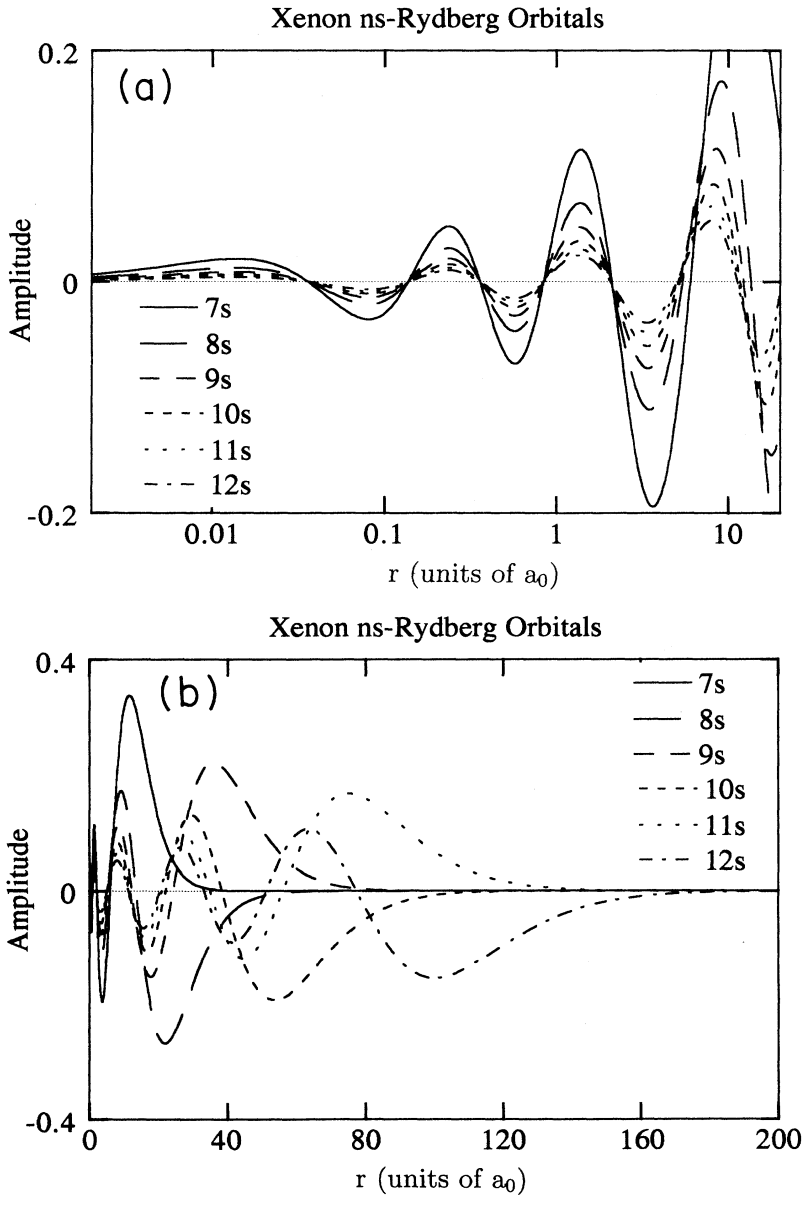

FIG. 5. Radial wave function of ns-Rydberg states of xenon. In (a) the radial coordinate is plotted on a logarithmic scale, (b) shows the wave functions at large distances.

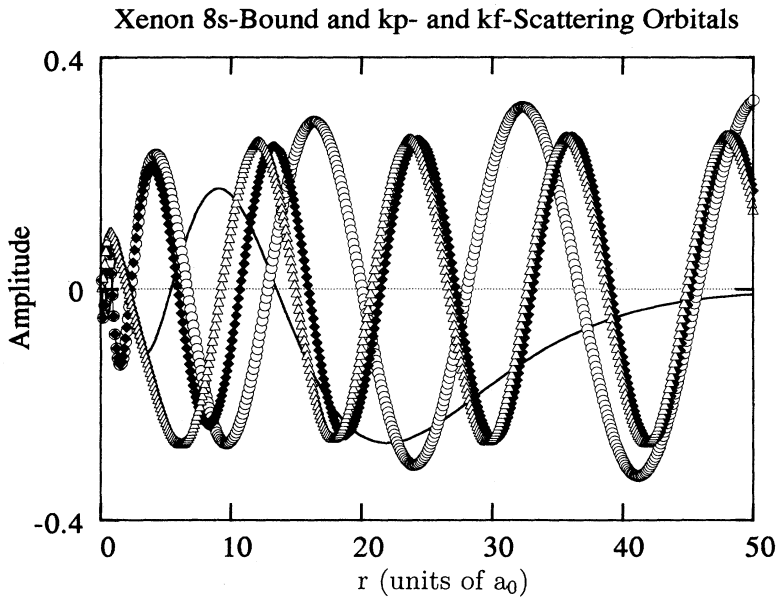

FIG. 6. The radial dependence of the 8*s*-wave function is shown together with the continuum wave functions εp and εf (open circles, $l=1$ at 1 eV; filled diamonds, $l=1$ at 3 eV; open triangles, $l=3$ at 3 eV).

result that the Cooper minima for the *ns*-Rydberg series members all appear at approximately the same scattering energy.

The convergence of Cooper minima to a single-scattering energy has been noted and discussed previously by Wang and Pratt [18] in the case of the *ns* subshells of excited uranium. They found that above a certain principle quantum number the energies of the Cooper minima became constant. We find this also to be the case in xenon.

In Fig. 5 we show the *ns* valence orbitals. The inner nodes of these orbitals are almost identical as shown in Fig. 5(a). In fact if we allow them to have the same initial slope at the origin [18] the amplitudes of the inner antinodes become identical also. The outer antinodes, shown in Fig. 5(b), rapidly extend far from the nucleus, with the distance between nodes growing rapidly. As *n* increases, the range over which these orbitals are the same, except for a scale factor, increases very quickly. This is because all these orbitals must be orthogonal to the same core and lower *n* orbitals. The photon energies used in these experiments are near 4 eV so that the final energy in the (3+1)-photon ionization processes leaves the continuum electron with approximately 3 eV.

In Fig. 6 we show the *p*- and *f*-scattering orbitals, superimposed on the 8*s* orbital, for scattering energies in this range. It can easily be seen that for radii beyond 10–15 a_0 the scattering orbitals for 3 eV oscillate much more rapidly than the Rydberg orbital. Therefore, the magnitude of the dipole transition moment is determined by the contribution nearer the core, where both the bound and continuum orbitals are varying with roughly the same local wavelength. The final values for these integrals is quite small, with negligible contribution from the outer portions of the bound-state wave functions due to the rapid oscillations of the scanning state. The situa-

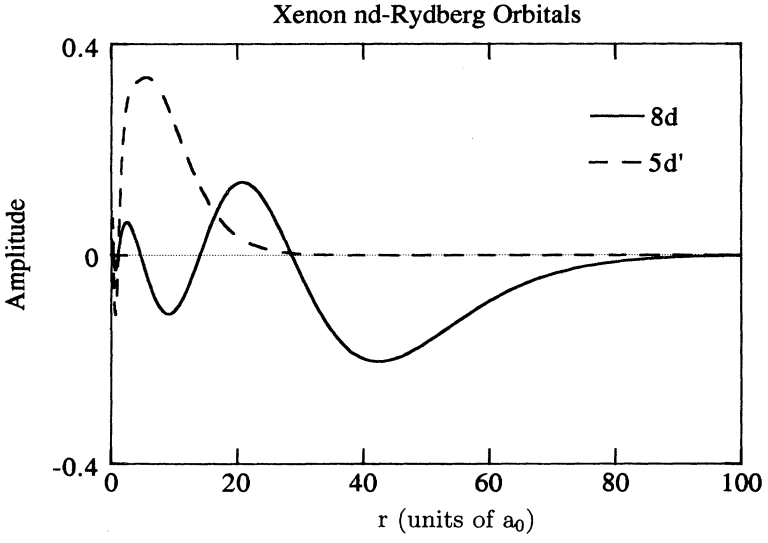

FIG. 7. Radial dependence of the 5*d'* and 8*d* orbitals.

tion is quite different for the bound $5d'$ orbital which has one large, broad maximum (and two nodes at very short r), resulting in much better overlap with the continuum wave function. The $5d'$ orbital is shown in Fig. 7, together with that for $8d$.

In Fig. 8 the dipole transition amplitudes are displayed as functions of the final electron scattering energy. In Fig. 8(a) we show the $ns \rightarrow \varepsilon p$ and $nd \rightarrow \varepsilon p$ results in Fig. 8(b) the $nd \rightarrow \varepsilon f$ amplitudes for a range of energy near threshold to 50 eV. We see all the $s \rightarrow p$ dipoles pass through zero within this range, the $7s$ changing sign first around 4 eV, then the rest following with successively smaller increments between the zeros. All have become positive by 16 eV. In the scattering energy range of interest in these experiments, the transition strengths for all these Rydbergs are quite small compared to those for the $d \rightarrow f$ transitions, particularly that for $5d' \rightarrow \varepsilon f$. Note in the latter case, the scattering energy of interest is smaller by the energy difference between the ion cores (1.31 eV) so the transition strength which is rising rapidly as threshold is approached is very large compared to those which populate the $^2P_{3/2}$ continua. Putting the calculated transition strengths in Eqs. (3) we obtain the ratios which are shown in Table II along with the experimental results and the MQDT predictions of the core character of the resonance.

The results for the ns levels are quite good, including a predicted maximum of the branching around $n=9,10$. The calculated branching fraction for the $7s'$ state is also dominated by the same $5d' \rightarrow \varepsilon f'$ component and is predicted also to produce mostly $^2P_{1/2}$ ions in disagreement with the observed result. The prediction for the $11s$ state

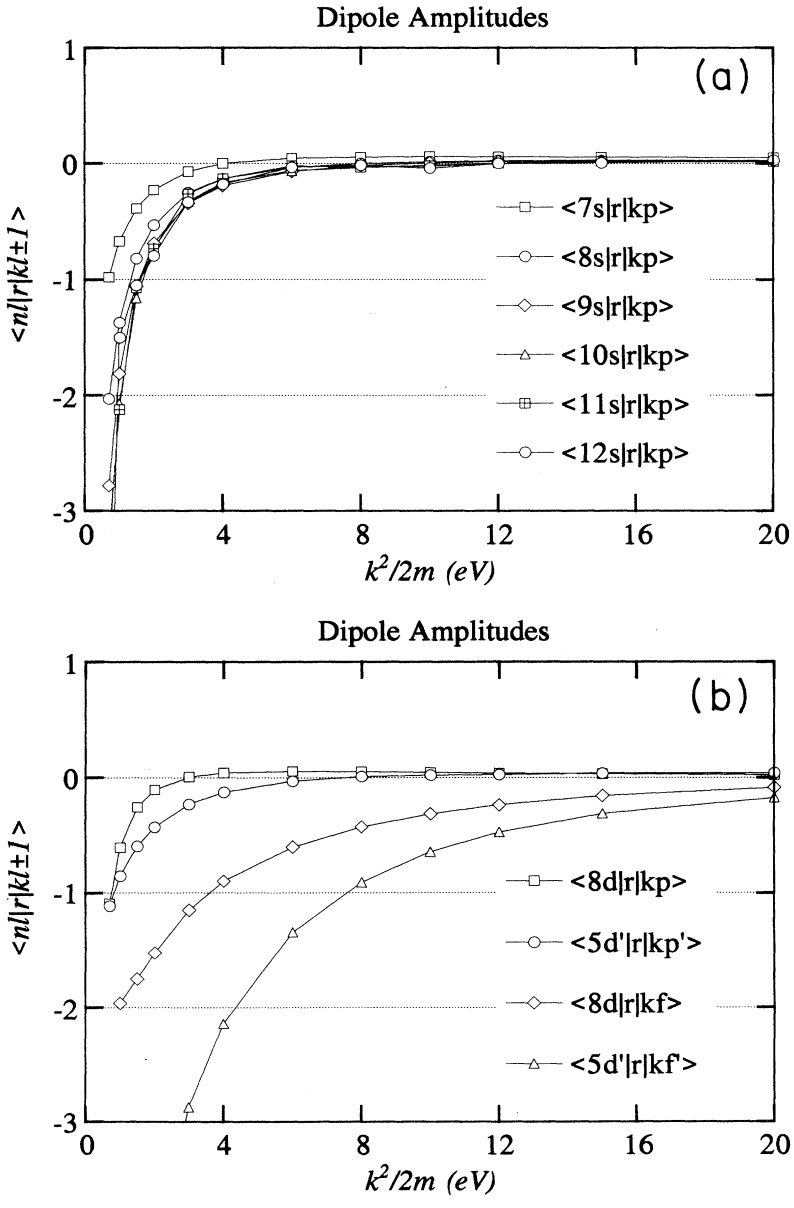

FIG. 8. Transition dipole amplitudes into p and f continua are shown for ns states (a) and the $8d$ and $5d'$ states in (b).

TABLE II. Comparison of observed and theoretical fraction of ions in the $Xe^+(^2P_{1/2})$ channel, following (3+1)-photon REMPI via *ns* states. The fifth column gives the MQDT predicted core admixture of $Xe^+(^2P_{1/2})$ as defined in Eq. (2a).

State label	Energy (cm^{-1})	Theory	Obs.	MQDT
$7s[3/2]_1$	85 440	0.67	0.57	0.007
$8s[3/2]_1$	90 932	0.50	0.62	0.006
$9s[3/2]_1$	93 422	0.88	0.91	0.084
$10s[3/2]_1$	94 787	0.89	0.63	0.063
$11s[3/2]_1$	95 591	0.77	0.17	0.163
$7s'[1/2]_1$	95 801	0.84	0.25	0.966
$12s[3/2]_1$	96 123	0.64	nm	0.110

is also comparatively poor. It is not clear why this disagreement exists for these two states, but one possible explanation is that the strong interaction between the *s* and *s'* manifolds due to the presence of the $7s'$ state at this energy may mean that the MQDT coefficients are more difficult to obtain with comparable reliability.

CONCLUSIONS

Multiphoton ionization of xenon via resonantly excited three-photon states shows a close correspondence between the final-state ion population and the degree of core mixing if the resonant intermediates belong to the *nd* and *nd'* Rydberg series. The reason for this correspondence is the similarity in the transition amplitudes from the *nd* and *nd'* configurations, which account for most of the character of the excited states. In sharp contrast, REMPI involving the *ns*-Rydberg members show preferential formation of $Xe^+(^2P_{1/2})$ although these members are nearly pure Rydberg states belonging to the $Xe^+(^2P_{3/2})$ core.

The numerical calculations support the interpretation of the unexpected propensity for ionizing into the opposite core as being due both to the large magnitude of the transition strengths of the minor *d'* components of the resonant state wave functions and the similarly small transition strengths for the dominant *ns* components for all the Rydberg levels. As predicted earlier by Wang and Pratt [18] it is a general feature of Rydberg series Cooper minima that as the principal quantum number becomes higher, the change in sign in the transition matrix element will tend to occur at the same scattering energy because the integrand is determined by the portion of the orbitals which become independent of *n* except for a normalization factor. The location of the zero of these matrix elements cannot depend on this normalization.

ACKNOWLEDGMENTS

Many helpful discussions with Dr. D. L. Huestis are greatly appreciated. K. C. K. would like to acknowledge helpful conversations with Dr. T. N. Rescigno and Professor C. H. Greene and to thank JILA for its kind hospitality while this work was being pursued. This research was supported by a grant from the National Science Foundation, PHY-9024710. C. B. acknowledges partial support by CNRS. T. A. F. acknowledges support through an NSF REU site grant at SRI (NSF-PHY-9300247).

[1] R. N. Compton, J. C. Miller, A. E. Carter, and P. Kruit, Chem. Phys. Lett. **71**, 87 (1980).
[2] P. Kruit, J. Kimman, H. G. Mueller, and M. J. Van der Wiel, J. Phys. B **16**, 937 (1983).
[3] K. Sato, Y. Achiba, and K. Kimura, J. Chem. Phys. **80**, 57 (1984).
[4] S. T. Pratt, P. M. Dehmer, and J. L. Dehmer, Phys. Rev. A **35**, 3793 (1987).
[5] E. Matthias, P. Zoller, D. S. Elliott, N. D. Piltch, and J. S. Smith, Phys. Rev. Lett. **50**, 1914 (1983).
[6] H. Helm, N. Bjerre, M. J. Dyer, D. L. Huestis, and M. Saeed, Phys. Rev. Lett. **70**, 3221 (1993).
[7] P. Lambropoulos, Adv. At. Mol. Phys. **12**, 87 (1976).
[8] C. J. Dash, Appl. Opt. **31**, 1146 (1992).
[9] K. T. Lu, Phys. Rev. A **4**, 579 (1971).
[10] A. L'Huillier, X. Tang, and P. Lambropoulos, Phys. Rev. A **34**, 2998 (1986).
[11] J. Geiger, Z. Phys. A **282**, 129 (1977).
[12] J. W. Cooper, Phys. Rev. **128**, 681 (1962).
[13] K. N. Huang and A. F. Starace, Phys. Rev. A **19**, 2335 (1979).
[14] H. A. Hyman, Appl. Phys. Lett. **31**, 14 (1977).
[15] K. J. McCann and M. R. Flannery, Appl. Phys. Lett. **31**, 599 (1977).
[16] S. T. Manson, C. J. Lee, R. H. Pratt, J. B. Goldberg, B. R. Tambe, and A. Ron, Phys. Rev. A **28**, 2885 (1983).
[17] F. Hermann and S. Skillman, *Atomic Structure Calculations* (Prentice-Hall, Englewood Cliffs, NJ, 1963).
[18] M. S. Wang and R. H. Pratt, Phys. Rev. A **29**, 174 (1984).

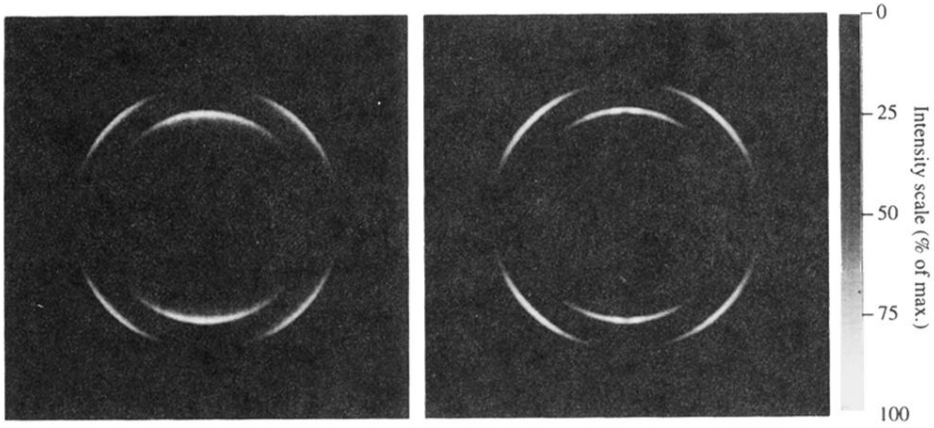

FIG. 1. Typical photoelectron image from four-photon ionization of xenon. The resonant intermediate in this case is $8d[1/2]_1$. The raw photoelectron image is shown on the left. The image on the right is the Abel-inverted image which shows the angular distribution of electrons. The radial coordinate is a measure of the electron velocity. The laser polarization is vertical, parallel to the screen.